

# NOISE-ROBUST ONE-BIT DIFFRACTION TOMOGRAPHY AND OPTIMAL DOSE FRACTIONATION

PENGWEN CHEN AND ALBERT FANNJIANG

**ABSTRACT.** This study presents a noise-robust framework for 1-bit diffraction tomography, a novel imaging approach that relies on intensity-only binary measurements obtained through coded apertures. The proposed reconstruction scheme leverages random matrix theory and iterative algorithms, including power iteration and shifted inverse power iteration, to effectively recover 3D object structures under high-noise conditions. Theoretical analysis highlights the de-noising capabilities of the 1-bit scheme, with numerical experiments validating its robustness across varying noise levels, projection densities, and mask configurations.

A key contribution is the investigation of dose fractionation, revealing optimal performance at a signal-to-noise ratio near 1, independent of the total dose. This finding addresses the dose-damage trade-off critical in radiation-sensitive imaging applications, such as biological microscopy. The study also explores the spectral properties of the reconstruction process, providing insights into algorithmic convergence and the interplay between eigenvector correlations and spectral gaps.

## 1. INTRODUCTION

Diffraction tomography is a distinct variant of tomographic imaging techniques that predominantly employs wave diffraction, as opposed to absorption, as the fundamental mode of object-wave interaction. At the heart of diffraction tomography is the goal to uncover the object's interior structure by acquiring scattered wavefield data from various orientations around the object. Unlike absorption-based methods, in this technique, both the phase and amplitude of the diffracted waves provide vital information about the object's internal structure. This technique is particularly useful in areas such as non-destructive testing, biomedical imaging, geophysics, and more, where the wavelength of the probing wave is on par with the dimensions of the object or inhomogeneity in the medium, resulting in diffraction phenomena.

In a traditional diffraction tomography setup, the complex-valued scattered wavefield, containing both magnitude and phase information, would be measured. However, in the case of intensity-only measurement, only the magnitude of the scattered wavefield is measured. This approach simplifies the detection process as it circumvents the challenge of phase measurement, which often requires complex and precise instruments like lenses and interferometers, especially in high-frequency settings.

Further down the ladder of measurement complexity is diffraction tomography with threshold-crossing intensity-only measurements where a binary representation of the diffracted wave's

---

Department of Applied Mathematics, National Chung Hsing University, Taichung, 402, Taiwan.  
Department of Mathematics, University of California, Davis, CA 95616, USA.

intensity inherently simplifies the data acquisition and processing. A certain threshold intensity level is predefined, and the sensor only records whether the intensity of the scattered wave is above or below this threshold.

This binary data is simpler to collect and process, and less sensitive to noise compared to full-waveform data. However, such thresholding inevitably leads to a loss of information about the object, making the subsequent image reconstruction process more challenging. Consequently, the choice to use 1-bit intensity-only measurements must carefully balance the benefits of reduced data requirements and increased simplicity against the loss of potentially valuable phase information.

The image reconstruction process typically involves solving an inverse problem to recover the object's properties from the binary data. Given the binary nature of the data, this is usually a non-linear and ill-posed problem. Traditional reconstruction techniques, like filtered backprojection or Radon inversion methods, which are suitable for high-precision measurements, may not work effectively for 1-bit intensity-only measurements due to their binary nature and the absence of phase information.

To give a context for the current work, let us briefly recall some key advances and insights in the related area of signal reconstruction of two-dimensional complex band-limited signals from *threshold crossings in the real and imaginary parts*.

On the one hand, at the Nyquist rate, a band-limited signals can be reconstructed from samples of infinite precision. On the other hand, a band-limited signal whose entire extension is irreducible is uniquely determined, up to some constant factor, by the sign information (real zero-crossings) of its real and imaginary parts, requiring essentially 2-bit information of the samples. While the former case has a robust performance with respect to sample imprecision, the latter case requires, in theory and practice, extreme accuracy in identifying zero crossings [7, 23, 28]. Furthermore, the choice of the threshold level can significantly impact the quality of the reconstruction, making it a crucial factor to consider in the design of such systems.

Therefore, in view of this instability in signal reconstruction from *approximate* information of zero-crossings, the task of tomographic phase retrieval with 1-bit threshold crossing is quite untenable.

A key component of our approach to mitigating the problem is a randomly coded aperture [9] resulting in coded diffraction patterns of greater diversity. The idea is motivated by a Gaussian random matrix theorem proved in [6].

**1.1. Plan and organization.** First in Section 2, we discuss the random matrix theorem motivating the present work and the noise reduction mechanism.

Next in Section 3 we discuss the power method and the shifted inverse power method for reconstruction with the discrete framework of tomography which is amenable to information-theoretical analysis as well as exact simulations [10, 11] (see Appendix A).

In Section 4, we define the Noise-to-Signal ratio (NSR) for 3D tomographic phase retrieval with the Poisson noise and in Section 5 we discuss our tomographic sampling scheme and, in particular, the selection of threshold for noisy data.

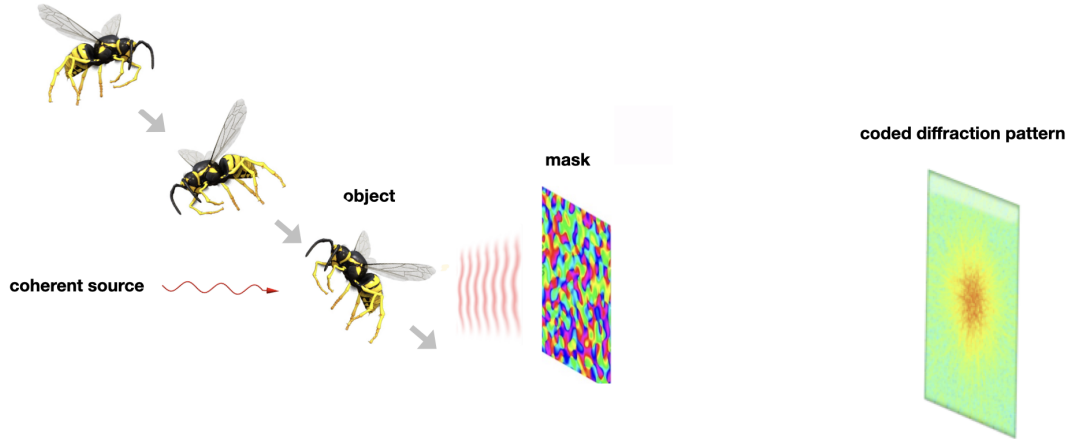


FIGURE 1. Diffraction patterns of an object in various orientations are measured with the same random mask

In Section 5 we show that with a sufficiently large number of projections the power method is more advantageous while with a small to moderate number of projections, the shifted inverse power method converges much faster and is more stable. The numerical performance of both power methods is robust to the complexity of the random mask used.

Finally in Section 6 we report numerical experiments with dose fractionation. The idea of dose fractionation emerged primarily in the context of electron microscopy, where highly sensitive samples are prone to radiation damage [15, 17, 20]. The core principle of dose fractionation is to split the total radiation dose into multiple, lower-intensity exposures rather than applying the entire dose in a single exposure. This technique balances the need for sufficient signal to image fine details with the need to limit radiation damage that can degrade or destroy the sample. Dose fractionation is an implicit assumption in the successful method of single-particle imaging in electron microscopy [12].

Likewise, by using fractionated doses and computationally averaging the resulting patterns, tomographic X-ray diffractive imaging can capture complete 3D structures with reduced risk of damaging the sample in each projection [19].

Surprisingly dose fractionation achieves the optimal performance at SNR near 1, independent of the total dose, which is the most significant finding of the paper.

## 2. RANDOM-MATRIX THEOREM

Consider the nonlinear signal model:  $b = |\mathcal{A}f_*|$ , where  $\mathcal{A} \in \mathbb{C}^{M \times N}$  is the measurement matrix and  $|\cdot|$  denotes entrywise modulus. We select a threshold to separate the “weak” signals, due to destructive interference, from the “strong” signals, due to constructive interference, as follows. Let  $I \subset \{1, \dots, N\}$  be the support set of the weak signals (to be determined) and  $I_c$  its complement such that  $b[i] \leq b[j]$  for all  $i \in I, j \in I_c$ . Denote the sub-row matrices with row indices in  $I$  and  $I_c$  by  $\mathcal{A}_I$  and  $\mathcal{A}_{I_c}$ , respectively.

The significance of the weak signal support  $I$  lies in the fact that  $I$  contains the best loci to “linearize” the problem since  $b_I$  is “small”. This motivates the least squares problem:

$$(1) \quad \min \{ \|\mathcal{A}_I f\|^2 : f \in \mathbb{C}^N, \|f\| = \|f_*\| \}.$$

A slightly simplified version of the theorem proved in [6] is the following.

**Theorem 2.1.** [6] *Let  $\mathcal{A}$  be an  $M \times N$  i.i.d. complex Gaussian matrix and  $f_{\min}$  a minimizer of (1). Suppose*

$$(2) \quad N < |I| \ll M \ll |I|^2.$$

*Then with an overwhelming probability, the relative error bound*

$$(3) \quad \|f_* f_*^* - f_{\min} f_{\min}^*\|_{\text{F}} / \|f_*\|^2 \leq c_0 \sqrt{|I|/M} \ll 1$$

*holds for some constant  $c_0$ , where  $\|\cdot\|_{\text{F}}$  denotes the Frobenius norm.*

In practice, it is convenient to consider the following surrogate:

$$(4) \quad \max \{ \|\omega \odot \mathcal{A}f\|^2 : f \in \mathcal{X}, \|f\| = \|f_*\| \}$$

where  $\omega$  is the indicator vector for  $I_c$ . The asymptotical equivalence between (1) and (4) as  $M \rightarrow \infty$  can be seen as follows.

As  $M \rightarrow \infty$ , the column vectors of  $\mathcal{A} = [a_{ij}]$  have nearly the same norm  $M^{1/2}$  (assume unit variance for each entry  $a_{ij}$ ) and are nearly mutually orthogonal in the sense that

$$M^{-1} \sum_{i=1}^M \bar{a}_{ij} a_{ik} \sim M^{-1/2} \rightarrow 0, \quad j \neq k.$$

In other words, we can think of  $M^{-1/2} \mathcal{A}$  as an isometry when  $M$  is much larger than  $N$ . By the isometry property

$$(5) \quad \|f\|^2 = M^{-1} \|\mathcal{A}_I f\|^2 + M^{-1} \|\mathcal{A}_{I_c} f\|^2,$$

minimizing  $\|\mathcal{A}_I f\|^2$  is equivalent to maximizing  $\|\mathcal{A}_{I_c} f\|^2$  over  $\{f : \|f\| = \|f_*\|\}$ .

**2.1. Noise robustness.** Let us consider some heuristic for de-noising effect of the 1-bit intensity-only scheme.

The noise level is measured by the noise-to-signal ratio (NSR), the reciprocal of signal-to-noise ratio (SNR), given by

$$(6) \quad \text{NSR} = (\text{SNR})^{-1} := \frac{\text{Total \# average non-signal photons}}{\text{Total \# signal photons}},$$

the reciprocal of the signal-to-noise ratio (SNR). At any given noise level, the  $I/I_c$ -membership of the indices near the threshold are least robust to noise while the membership of the extreme (very strong or very weak) indices are most robust to noise.

We want to show that these robust indices and the corresponding row vectors also play the strongest role in the synthesis of  $f_{\max}$  and  $f_*$ .

Let  $a_j^T$  denote the  $j$ -th row vector of  $\mathcal{A}$ . We can write

$$(7) \quad \mathcal{A}^*(\omega \odot \mathcal{A}) = \sum_{j \in I_c} \overline{a_j} a_j^T,$$

the sum of rank-one projections restricted to  $I_c$ . Here and below, the over-line notation denotes the complex conjugation.

By Theorem 2.1, the leading eigenvector  $f_{\max}$  of the Gram matrix (7) approximates the true object  $f_*$ , so we have

$$(8) \quad f_* \sim \sum_{j \in I_c} \overline{a_j} (a_j^T f_*)$$

which can be interpreted as a linear decomposition of  $f_*$  into its features  $\{\overline{a_j} : j \in I_c\}$  with coefficients  $a_j^T f_*$ . As expected, the larger the **noiseless** data  $|a_j^T f_*|$ , the more significant the corresponding feature  $\overline{a_j}$  in the synthesis of  $f_*$ .

Thereby lies the de-noising mechanism of the one-bit scheme. Our numerical simulations below provide ample evidence for the plausibility of this idea.

### 3. POWER ITERATION AND INVERSE POWER ITERATION

Introducing the projection  $\mathcal{P}_{\mathcal{X}}$  unto the object space  $\mathcal{X}$ , we can rewrite (4) as

$$(9) \quad \arg \max \{ \langle g, \mathcal{P}_{\mathcal{X}} \mathcal{A}^* \text{diag}(\omega) \mathcal{A} \mathcal{P}_{\mathcal{X}} g \rangle : g \in \mathbb{C}^N, \|g\| = \|f_*\| \}$$

where we have used the fact that  $\omega^2 = \omega$ . Here we assume that  $\mathcal{X}$  is a linear vector space resulting from, e.g. a more restrictive support constraint due to zero-padding in the mathematical set-up.

Viewed as the Rayleigh quotient for the leading eigenvector(s) of the positive semidefinite matrix  $\mathcal{P}_{\mathcal{X}} \mathcal{A}^* \text{diag}(\omega) \mathcal{A} \mathcal{P}_{\mathcal{X}}$ , (9) suggests the power iteration for solution

$$(10) \quad g^{(k+1)} = (\mathcal{P}_{\mathcal{X}} \mathcal{A}^* \text{diag}(\omega) \mathcal{A} \mathcal{P}_{\mathcal{X}})^k g^{(1)} \|f_*\| / \|(\mathcal{P}_{\mathcal{X}} \mathcal{A}^* \text{diag}(\omega) \mathcal{A} \mathcal{P}_{\mathcal{X}})^k g^{(1)}\|,$$

for  $k \in \mathbb{N}$ .

Replace the constraint  $\|f\| = \|f_*\|$  in (4) with  $\|\mathcal{A}f\| = \|b\|$ . An alternative formulation can be developed in terms of the transform domain variables  $z$  as follows. Let  $\mathcal{A}^\dagger$  be the pseudo-inverse of  $\mathcal{A}$  in the object space  $\mathcal{X}$  and  $\mathcal{P} = \mathcal{A} \mathcal{A}^\dagger$  the orthogonal projection onto the space  $\mathcal{AX}$ .

Replacing  $\mathcal{A}f$  by  $z$  and  $f$  by  $\mathcal{A}^\dagger z$ , we can formulate (4) as the following optimization problem

$$(11) \quad \begin{aligned} & \arg \max \{ \|\text{diag}(\omega) z\|^2, z \in \mathcal{AX}, \|z\| = \|b\| \} \\ &= \arg \max \{ \|\text{diag}(\omega) \mathcal{P} z\|^2 : z \in \mathbb{C}^M, \|z\| = \|b\| \} \\ &= \arg \max_{\|z\|=\|b\|} \langle z, \mathcal{P}_\omega z \rangle, \quad \mathcal{P}_\omega := \mathcal{P} \text{diag}(\omega) \mathcal{P} \end{aligned}$$

which is the Rayleigh quotient for  $\mathcal{P}_\omega$ 's leading eigenvector. This leads to the power iteration,

$$(12) \quad z^{(k+1)} = \mathcal{P}_\omega z^{(k)} \|b\| / \|z^{(k)}\|, \quad k \in \mathbb{N}.$$

Using  $f^{(k)} = \mathcal{A}^\dagger z^{(k)}$  and  $\mathcal{A}^\dagger = \mathcal{A}^\dagger \mathcal{A} \mathcal{A}^\dagger$ , we have

$$(13) \quad f^{(k+1)} = \mathcal{A}^\dagger \text{diag}(\omega) \mathcal{A} f^{(k)} \|b\| / \|\mathcal{A} f^{(k)}\|, \quad k \in \mathbb{N}.$$

See Alg. 1.

---

**Algorithm 1: The Power Method**

---

- 1 **Input:** The indicator vector  $\omega$  for  $I_c$ ;
  - 2 **Random initialization:**  $\mathbf{f}^{(1)} = \mathbf{f}_{\text{rand}}$ ,  $z^{(1)} = \mathcal{A} \mathbf{f}^{(1)}$ .
  - 3 **Loop:**
  - 4 **for**  $k = 1 : k_{\text{max}} - 1$  **do**
  - 5      $\mathbf{f}^{(k+1)} \leftarrow \mathcal{A}^\dagger(\omega \odot z^{(k)})$ ;
  - 6      $z^{(k+1)} \leftarrow \mathcal{A} \mathbf{f}^{(k+1)} \|b\| / \|\mathcal{A} \mathbf{f}^{(k+1)}\|$
  - 7 **end**
  - 8 **Output:**  $\mathbf{f}^{k_{\text{max}}}$ .
- 

3.1. **Shifted inverse power iteration.** The power iteration (13) can be written as

$$(14) \quad \lambda^{(k+1)} \mathcal{R}^* \mathcal{R} f^{(k+1)} = \mathcal{R}^* \mathcal{Q}^* \text{diag}(\omega) \mathcal{Q} \mathcal{R} f^{(k)}, \quad \lambda^{(k+1)} := \|\mathcal{A} f^{(k)}\| / \|b\|,$$

which computes the dominant eigenvector  $\mathbf{f}_{\text{max}}$  of

$$(15) \quad \mathcal{A}^\dagger \text{diag}(\omega) \mathcal{A} = (\mathcal{R}^* \mathcal{R})^{-1} \mathcal{R}^* \mathcal{Q} \text{diag}(\omega) \mathcal{Q} \mathcal{R}.$$

Hence, for some  $\lambda$  we have

$$(16) \quad \lambda \mathcal{R}^* \mathcal{R} \mathbf{f}_{\text{max}} = \mathcal{R}^* \mathcal{Q}^* \text{diag}(\omega) \mathcal{Q} \mathcal{R} \mathbf{f}_{\text{max}}.$$

Let

$$(17) \quad \mathcal{S}_\omega := \mathcal{R}^* \mathcal{Q}^* \text{diag}(\omega) \mathcal{Q} \mathcal{R}, \quad \mathcal{S} := \mathcal{R}^* \mathcal{Q}^* \mathcal{Q} \mathcal{R} = \mathcal{R}^* \mathcal{R}.$$

Then  $\lambda$  is a generalized eigenvalue of the symmetric-definite pair  $\{\mathcal{S}_\omega, \mathcal{S}\}$ , with the corresponding generalized eigenvector

$$(18) \quad \mathbf{f}_{\text{max}} = \arg \max_{\mathbf{f}} \frac{\langle \mathbf{f}, \mathcal{S}_\omega \mathbf{f} \rangle}{\langle \mathbf{f}, \mathcal{S} \mathbf{f} \rangle}$$

where  $\mathbf{f}$  must be further restricted to the range of  $\mathcal{S}$  if  $\mathcal{S}$  is singular. Assume that  $\mathcal{S}$  is nonsingular for simplicity. Since both  $\mathcal{S}_\omega, \mathcal{S}$  are positive semi-definite and  $\mathcal{S}_\omega \preceq \mathcal{S}$ , then eigenvalues of  $\mathcal{S}^{-1} \mathcal{S}_\omega$  lie in  $[0, 1)$ . Let  $\lambda_1 > \lambda_2$  be the leading two eigenvalues. The convergence rate of the power iteration is given by  $\lambda_2 / \lambda_1$ .

When both  $\lambda_1$  and  $\lambda_2$  are close to 1, the power iteration converges slowly. An effective way to speed up the convergence is to adopt the shifted inverse power iteration related to  $I - \mathcal{S}^{-1} \mathcal{S}_\omega$ . Let  $\mu$  be the dominant eigenvalue given by

$$(19) \quad \mu = \max_{\mathbf{f}} \frac{\langle \mathcal{S} \mathbf{f}, (\mathcal{S} - \mathcal{S}_\omega)^{-1} \mathcal{S} \mathbf{f} \rangle}{\langle \mathbf{f}, \mathcal{S} \mathbf{f} \rangle}$$

Observe that

$$\begin{aligned}
(I - \mathcal{S}^{-1}\mathcal{S}_\omega)^{-1} &= (I - (\mathcal{R}\mathcal{R}^*)^{-1}\mathcal{R}^*\mathcal{Q}^*\text{diag}(\omega)\mathcal{Q}\mathcal{R})^{-1} \\
&= ((\mathcal{R}^*\mathcal{R})^{-1}\mathcal{R}^*(I - \mathcal{Q}^*\text{diag}(\omega)\mathcal{Q})\mathcal{R})^{-1} \\
&= (\mathcal{R}^*\mathcal{Q}^*\text{diag}(1 - \omega)\mathcal{Q}\mathcal{R})^{-1}\mathcal{R}^*\mathcal{R}.
\end{aligned}$$

The shifted inverse iteration consists of generating  $\mathbf{f}^{(k+1)}$  from solving the equation,

$$(20) \quad \mu^{(k+1)}(\mathcal{R}^*\mathcal{Q}^*(1 - \text{diag}(\omega))\mathcal{Q}\mathcal{R})\mathbf{f}^{(k+1)} = \mathcal{R}^*\mathcal{R}\mathbf{f}^{(k)}, \quad \mu^{(k+1)} \in \mathbb{R}.$$

---

**Algorithm 2: The Inverse Power Method**

---

- 1 **Input:** The indicator vector  $\omega$  for  $I_c$ .
  - 2 **Random initialization:**  $\mathbf{f}^{(1)} = \mathbf{f}_{\text{rand}}$ .
  - 3 **Loop:**
  - 4 **for**  $k = 1 : k_{\text{max}} - 1$  **do**
  - 5 | Apply preconditioned CG to solve  $\mathbf{f}^{(k+1)}$  from (20).
  - 6 **end**
  - 7 **Output:**  $\mathbf{f}^{k_{\text{max}}}$ .
- 

Algorithm 2 has several advantages over Algorithm 1. First, both algorithms converge slowly when the spectral gap  $|\lambda_1 - \lambda_2|$  is close to zero but they do it at different rates. Observe that  $\lambda$  in (16) and  $\mu$  in (19) are related by  $\mu = (1 - \lambda)^{-1}$ . Hence the convergence rate of the shifted inverse iteration is given by  $(1 - \lambda_1)/(1 - \lambda_2)$ , which may be significantly less than  $\lambda_2/\lambda_1$  for  $\lambda_1, \lambda_2$  close to 1.

Second, when conjugate gradient methods(CG) are used to solve (14) or (20), the condition number is a crucial factor in determining the convergence speed of CG. Let the spectrum of  $\mathcal{S}^{-1}\mathcal{S}_\omega$  lie in some interval  $[\lambda_{\min}, \lambda_{\max}] \subset [0, 1)$ . Then the spectrum of  $(I - \mathcal{S}^{-1}\mathcal{S}_\omega)^{-1}$  lies in  $[(1 - \lambda_{\min})^{-1}, (1 - \lambda_{\max})^{-1}]$ . Empirically  $\lambda_{\max}$  is away from 1 and  $\lambda_{\min} \approx 0$ . Hence the system (20) has a much better condition number than the system in (14), improving the performance of the conjugate gradient method.

In the appendices, we describe an efficient algorithm for computing the pseudo-inverse  $\mathcal{R}^\dagger$  and  $\mathcal{A}^\dagger$  as well as the implementation of (20) in the context of diffraction tomography. The shifted inverse power iteration is summarized in Alg. 2.

#### 4. NOISE-TO-SIGNAL RATIO (NSR)

Photon noise, also called shot noise, is due to the statistical nature of photon emission and detection. When light passes through a phase mask and creates a diffraction pattern, the photon noise in that pattern is fundamentally dictated by the number of photons detected at each point in the pattern.

Photon noise is commonly described by the Poisson distribution such that the noisy intensity data vector  $\tilde{b}^2$  has as the noise components the independent Poisson random variables with the means equal to the noiseless components. To introduce the Poisson noise into our mathematical set-up, let  $b^2 = |\mathcal{A}f_*|^2$  as before but consider  $sb^2$  to be the noiseless intensity data with an adjustable scale factor  $s > 0$  representing the strength of illumination.

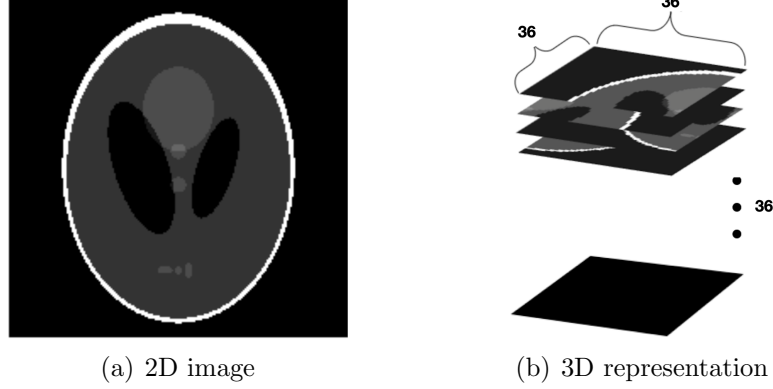


FIGURE 2.  $216 \times 216$  image  $\implies 36 \times 36 \times 36$  object.

Denote the intensity fluctuation by  $z = (z_j)$ . The (deterministic) noise photon count is  $\sum_j |z_j|$  and the total average noise photon count is given by

$$(21) \quad \sum_j \mathbb{E}|z_j| \quad \text{or more conveniently} \quad \sum_j \sqrt{\mathbb{E}|z_j|^2} = \left\| \sqrt{\mathbb{E}|z_j|^2} \right\|_1$$

where  $\|\cdot\|_1$  denotes the L1-norm of the vector. In the case of Poisson noise,  $z = \tilde{b}^2 - sb^2$  and hence the total number of average noise photons is given by  $\left\| \sqrt{\mathbb{E}(\tilde{b}^2 - sb^2)^2} \right\|_1$ . In other words, the NSR (6) can be conveniently defined as

$$(22) \quad \text{NSR} = (\text{SNR})^{-1} := \frac{\left\| \sqrt{\mathbb{E}(\tilde{b}^2 - sb^2)^2} \right\|_1}{s\|b^2\|_1} = \frac{\left\| \sqrt{\text{var}(\tilde{b}^2)} \right\|_1}{\|\mathbb{E}(\tilde{b}^2)\|_1}.$$

Notice that NSR is exactly the reciprocal of Signal-to-Noise Ration (SNR). By a straightforward calculation with the Poisson distribution, we have

$$(23) \quad \text{NSR} = (\text{SNR})^{-1} = \frac{\|b\|_1}{\sqrt{s}\|b^2\|_1}.$$

## 5. TESTING THE ALGORITHMS

In our simulations the mask phases  $\phi$  are independent uniform random variables over  $[0, 2\pi)$ . We will also test 2-phase and 4-phase random masks.

To aid visualization, we construct the *complex-valued* 3D object from the  $216 \times 216$  phantom (Fig. 2 (a)) by partitioning the real-valued phantom image into 36 pieces, each of which is  $36 \times 36$  and stacking them into a  $36 \times 36 \times 36$  cube (Fig. 2(b)). We then randomly modulate the phase of each voxel. The resulting 3D object is called 3D randomly phased phantom (RPP). We shall refer to the corresponding 2D randomly phased phantom as the flattened version of the 3D object.



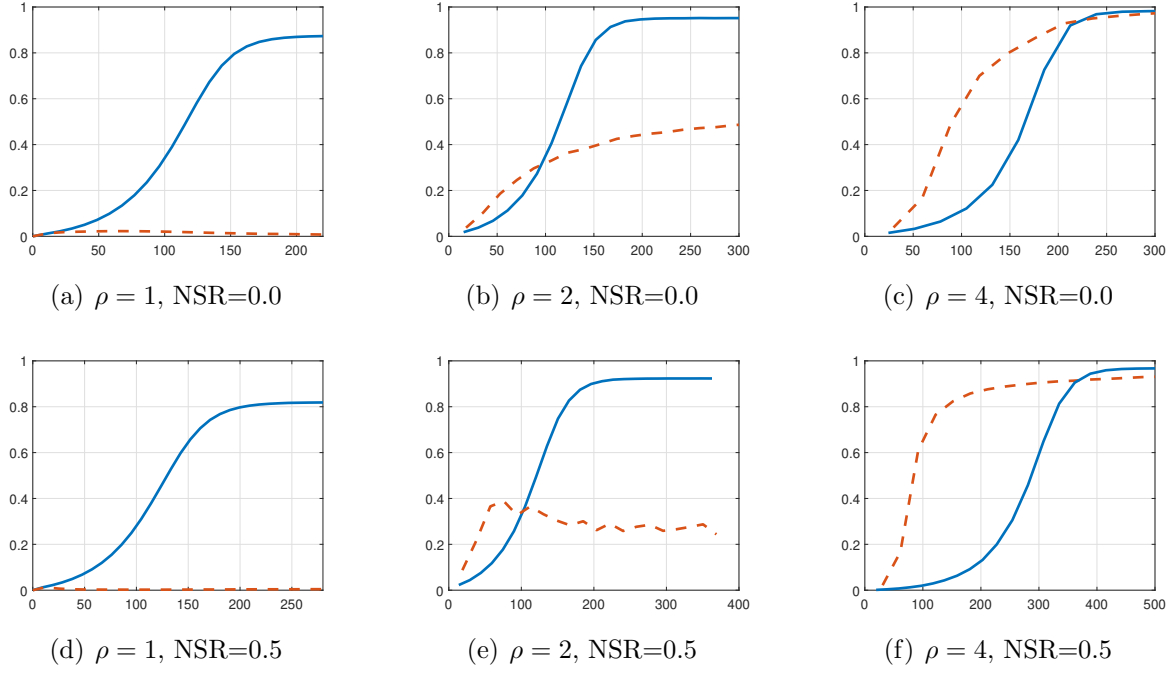


FIGURE 3. Correlation versus computation time (in second) by simple power method (dashed line) and inverse power method (solid line).

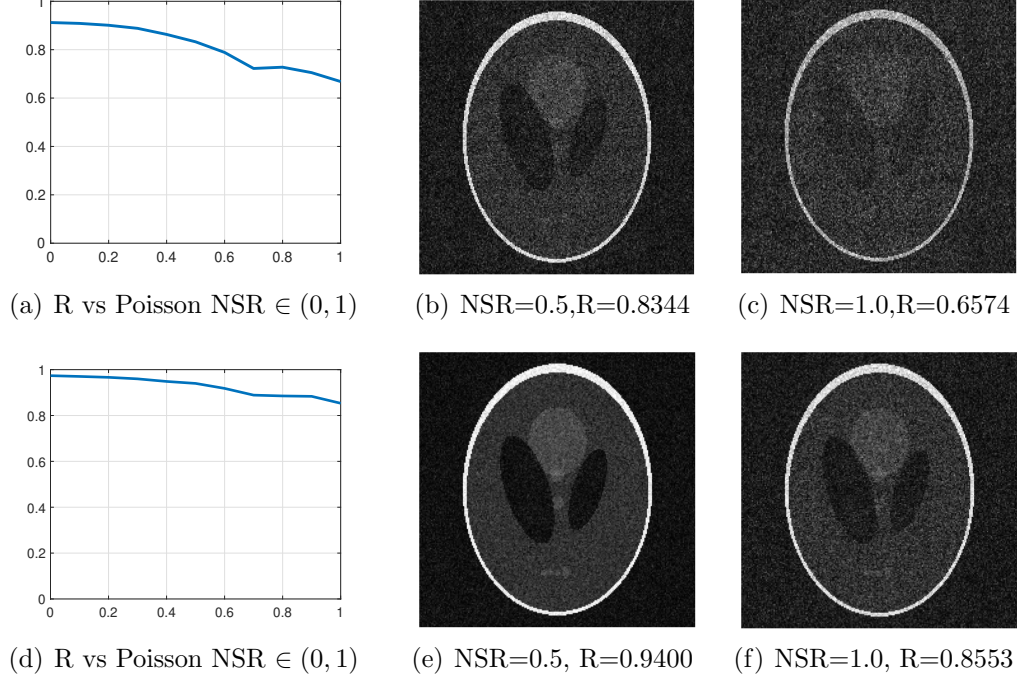


FIGURE 4. The magnitude  $|f|$  of the flattened reconstruction with  $\rho = 1$  (top) and  $\rho = 2$  (bottom). Different direction sets  $\mathcal{T}$  are independently selected for different NSRs.

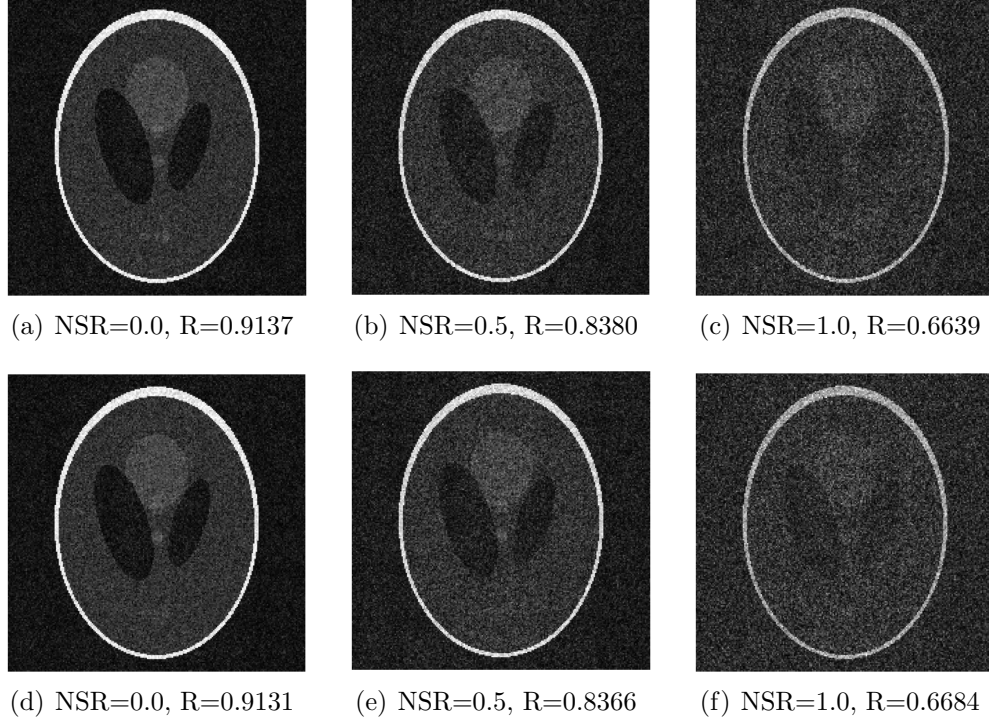


FIGURE 5. Flattened reconstructed magnitude with  $\rho = 1$  and with a 4-phase (top) and 2-phase (bottom) random mask at various Poisson NSRs.

In addition to the “eye-ball” metric, we also show the absolute correlation between  $f_*$  and reconstruction  $f$  given by

$$R(f, f_*) := \frac{|f^* f_*|}{\|f\| \|f_*\|}$$

which is analogous to the structure comparison function in the structural similarity index measure ([27], eq. (10)).

In our numerical results below, the absolute correlation largely corroborates with the visual quality of the reconstruction.

We use the reconstruction scheme (12) with the threshold selected separately for each coded diffraction pattern  $j = 1, \dots, m$  according to the guideline:

- For small NSR, Theorem 2.1 suggests a small value of  $|I_j|/p^2 < \frac{1}{2}$
- For large NSR, we adopt the median rule, i.e.  $|I_j|/p^2 = \frac{1}{2}$

where  $I_j$  is the index set of weaker signals in the  $j$ -th coded diffraction pattern. Specifically, we adopt the rule

$$(24) \quad |I_j|/p^2 = \min(1/4 + \text{NSR}/4, 1/2)$$

which is consistent with the condition (2).

To avoid the missing cone problem in tomography, we consider  $m = 3\rho n$  more or less evenly distributed random directions with the adjustable parameter  $\rho > 0$  (see (48) in Appendix

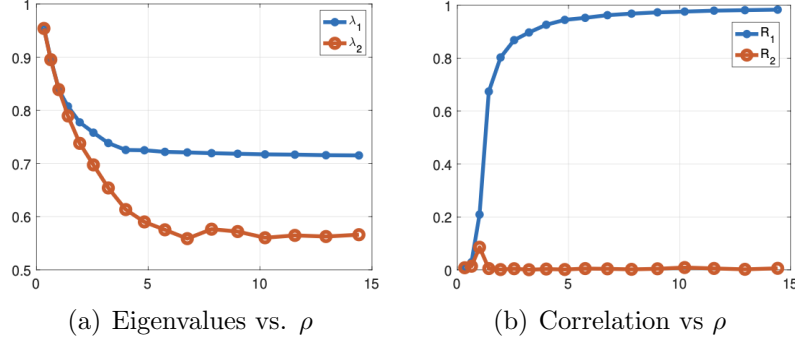


FIGURE 6. (a) The two leading eigenvalues and (b) the correlations as function of  $\rho$  at NSR=1 where  $R_1$  and  $R_2$  are respective correlations of the two leading eigenvectors with the original object.

A). According to [10, 11], a non-degenerate set of  $n + 1$  directions is the minimum requirement for discrete tomography with noiseless data. For 1-bit diffraction tomography with highly noisy data, however, one should deploy a larger set of directions for any reasonable reconstruction.

First let us compare the convergence rates of Algorithm 1 and Algorithm 2. Figure 3 shows the convergence comparison for various NSRs and  $\rho$ 's. The lesson is that with a small to moderate number of projections, Algorithm 2 converges much faster and is more stable while, with a large number of projection, Algorithm 1 has an advantage.

Figure 4 shows a few flattened reconstructions by Algorithm 2 with  $\rho = 1$  and  $\rho = 2$  in (48). As expected, the correlation increases with  $\rho$  and decreases with NSR.

Next we test the performance with a 4-phase random mask inspired by the quarter phase plate for X-rays or the quadrature phase shift keying used in communication systems. In other words, the mask phases are independent uniform variables in  $\{\pm\pi/2, \pm\pi\}$ . For further comparison, we also test the performance with the 2-phase random mask with phase as the Bernoulli random variables from  $\{\pm\pi\}$ .

By comparing the correlation at the same  $\rho$  and NSR in Figure 5 and 4 we see little difference between the performances of the 2-phase, 4-phase and the original masks.

We also compute the second leading eigenvector of  $\mathcal{S}^{-1}\mathcal{S}_\omega$  to shed a light on the relation between the convergence behavior and the spectral gap. To this end, we employ the Krylov subspace methods, described in Appendix E, to extract the second leading eigenvector.

Figure 6(a) shows that the spectral gap initially increases with  $\rho$  and then saturates after  $\rho > 5$  for NSR=1 and Figure 6(b) shows that the reconstruction correlation sharply rises plateauing after  $\rho > 5$ .

## 6. OPTIMAL DOSE FRACTIONATION

According to Henderson [16], “Radiation damage is the main problem which prevents the determination of the structure of a single biological macromolecule at atomic resolution using

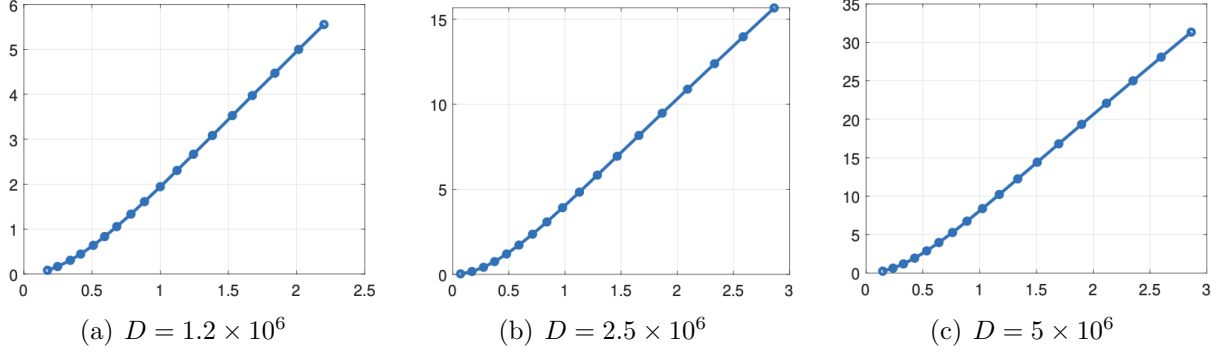


FIGURE 7.  $\rho$  versus NSR with different  $D$ 's.

any kind of microscopy. This is true whether neutrons, electrons or X-rays are used as the illumination.”

In other words, when it comes to single molecule imaging, the resolution is damage-limited, instead of diffraction-limited. The related dose-resolution scaling behaviors have been intensively studied [18, 25].

Despite these advances, a clear guideline for the best strategy of dose fractionation is yet to emerge. In this section, we present the surprising behavior of optimal dose fractionation with 1-bit measurement.

For dose fractionation experiments, we decompose the noisy signal  $\tilde{b}^2$  into the mean signal  $sb^2$  and the fluctuation  $z := \tilde{b}^2 - sb^2$ . Because  $\tilde{b}^2$  is a random vector, we use its root mean square value

$$(25) \quad D := \left\| \sqrt{\mathbb{E}(\tilde{b}^4)} \right\|_1 = \left\| \sqrt{s^2 b^4 + \mathbb{E}(z^2)} \right\|_1$$

as the dose metric. For the Poisson statistics,  $\mathbb{E}(z^2) = sb^2$  and hence

$$(26) \quad D = \left\| \sqrt{s^2 b^4 + sb^2} \right\|_1 = \sqrt{s} \|b\sqrt{sb^2 + 1}\|_1.$$

To find the dependence of the number  $m = 3\rho n$  of projections on NSR for a fixed dose, we need to solve the two nonlinear equations, (26) and (23).

Observe that NSR is primarily an (explicit) function of  $s$ , not  $m$ , while  $D$  depends linearly on  $m$  and nonlinearly on  $s$ . The solution of (26) and (23) takes the form of  $(\rho, s)$  as a function of NSR and  $D$  as shown in Figure 7 which can be roughly understood as follows.

For  $s$  large (small NSR),  $\sqrt{s^2 b^4 + sb^2} \sim sb^2$  and  $D \sim s \|b^2\|_1$ . Combining (22), we have

$$(27) \quad m \sim \|b\|_1 \sim (\text{NSR})^2 \cdot D \frac{\|b^2\|_1}{\|b\|_1}$$

with the right hand side roughly independent of  $m$ .

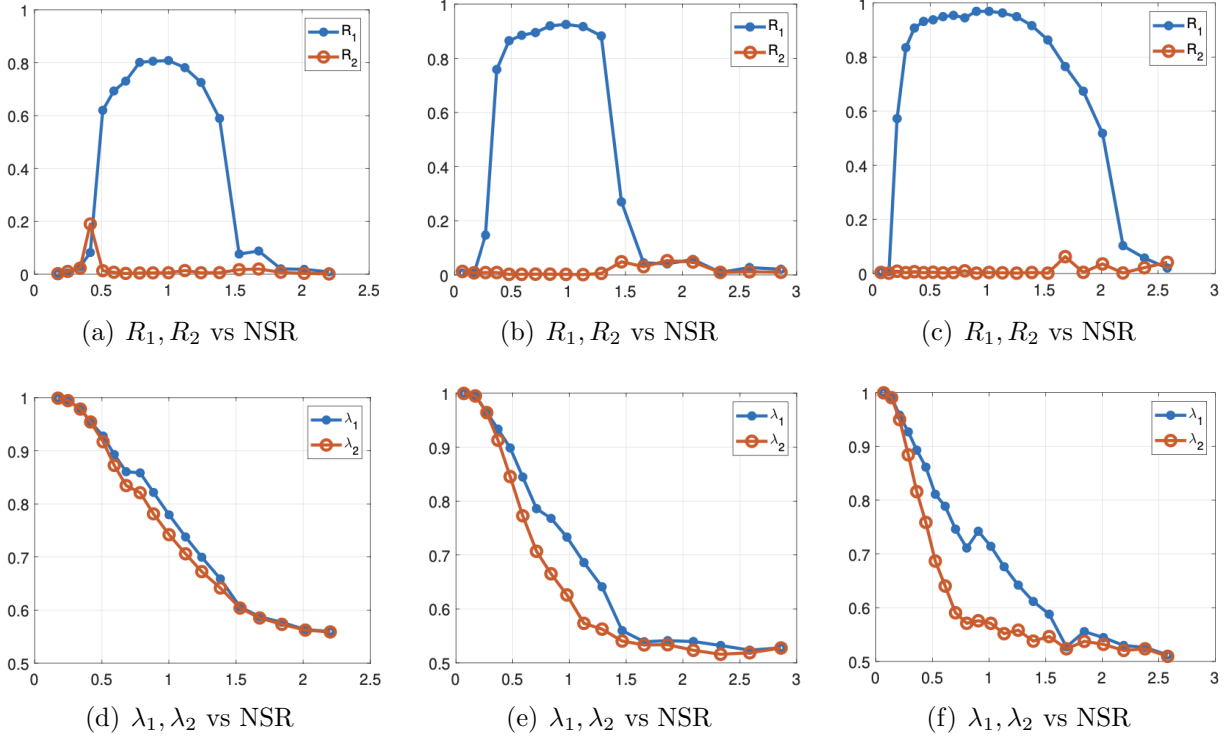


FIGURE 8. Correlations and eigenvalues vs NSR with a fixed (a)(d)  $D = 1.2 \times 10^6$ ; (b)(e)  $D = 2.5 \times 10^6$ ; (c)(f)  $D = 5 \times 10^6$ .

For  $s$  small (large NSR),  $\sqrt{s^2 b^4 + s b^2} \sim \sqrt{s} b$  and  $D \sim \sqrt{s} \|b\|_1$ . Combining (22), we have

$$(28) \quad m \sim \|b\|_1 \sim \text{NSR} \cdot D \frac{\|b^2\|_1}{\|b\|_1}$$

with the right hand side roughly independent of  $m$ .

The transition between the two regimes happens approximately at  $s b^2 = \sqrt{s} b$  or

$$(29) \quad s \|b^2\|_1 = \sqrt{s} \|b\|_1,$$

implying that  $\text{NSR} = 1$  is the transition point. As NSR increases from a low level (large  $s$ ), the number of projections  $m$  increases quadratically (according to (27)). The growth rate of projections reaches the plateau level

$$D \frac{\|b^2\|_1}{\|b\|_1}, \quad \text{for } \text{NSR} \geq 1.$$

We test the shifted inverse power method at three levels of dose:  $D = 1.2 \times 10^6, 2.5 \times 10^6, 5 \times 10^6$ , resulting in the root mean square number of photons per **voxel**

$$(30) \quad D/V = 25.7, 53.6, 107.2 \quad \text{photon/voxel}, \quad V := n^3.$$

Let  $R_1$  (resp.  $R_2$ ) denote the correlation between the true object and the leading (resp. the second leading) eigenvector. The results are shown in Figure 8 whose top row depicts  $R_1$

and  $R_2$ , and the bottom row  $\lambda_1, \lambda_2$ , both as function of NSR with the total dose fixed at three levels. The message is clear: the optimal dose fraction for all three levels of  $D$  happens around  $\text{NSR} = 1$  where the spectral gap is also the largest.

## 7. CONCLUSION

This work demonstrates the feasibility and robustness of 1-bit diffraction tomography in handling high-noise environments, achieving significant performance using coded apertures and advanced reconstruction techniques. By leveraging random matrix theory and iterative methods such as the power and shifted inverse power iterations, the study highlights the effective de-noising mechanisms inherent in the proposed approach. The adaptability of the proposed method is further highlighted through its performance with different mask configurations, including 2-phase and 4-phase random masks, which show comparable effectiveness to the original random mask design.

Furthermore, the results reveal the critical role of dose fractionation in optimizing performance while balancing noise suppression and sample integrity. The discovery of optimal performance near  $\text{SNR} = 1$  provides a valuable guideline for practical implementations, especially in applications constrained by radiation damage, such as biological imaging. This finding bridges the gap between dose minimization and effective signal recovery, offering a robust solution to the dose-damage trade-off prevalent in radiation-sensitive imaging applications.

Additionally, the spectral analysis of the reconstruction process uncovers the interplay between eigenvector correlations and spectral gaps, providing a deeper understanding of algorithmic convergence behaviors.

Interestingly the surprising effect of optimal dose fractionation near  $\text{SNR} = 1$  is not limited to 1-bit diffraction tomography. For example, similar effect persists in diffraction tomography with full intensity measurements. We will report the results of optimal dose fractionation for general tomographic modals in an upcoming article.

## APPENDIX A. DISCRETE TOMOGRAPHY

In this appendix, we recall the discrete framework of diffraction tomography developed in [11] and connect it to the matrix setting of Theorem 2.1.

The discrete framework is a discretization of the continuum model often called the high-frequency Born approximation used in cryo-electron microscopy [12] and X-ray diffractive imaging [19]. See [11] for the closely related high-frequency Rytov approximation.

In the continuum setting, the scattered exit waves modeled by the X-ray transform of  $f$  undergo propagation and then are detected by detectors at far-field.

In a diffraction-limited imaging system with the wavelength  $\lambda$ , the resolution length is roughly  $\lambda/2$ . Adopting a discrete framework for the X-ray transform, we set the grid spacing  $\lambda/2$ . For simplicity, let  $\lambda = 2$  so the grid spacing is 1.

Let  $\llbracket k, l \rrbracket$  denote the integers between and including the integers  $k$  and  $l$ . Let  $O_n$  denote the class of discrete complex-valued objects

$$(31) \quad O_n := \{f : f(i, j, k) \in \mathbb{C}, (i, j, k) \in \mathbb{Z}_n^3; f(i, j, k) = 0, (i, j, k) \notin \mathbb{Z}_n^3\}$$

where

$$(32) \quad \mathbb{Z}_n = \begin{cases} \llbracket -n/2, n/2 - 1 \rrbracket & \text{if } n \text{ is an even integer;} \\ \llbracket -(n-1)/2, (n-1)/2 \rrbracket & \text{if } n \text{ is an odd integer.} \end{cases}$$

To fix the idea, we consider the case of odd  $n$  in the paper.

Following the framework in [1] we discretize the projection geometry as follows.

We define three families of line segments, the  $x_1$ -lines,  $x_2$ -lines, and  $x_3$ -lines. The  $x_1$ -lines, denoted by  $\ell_{(1, \alpha, \beta)}(c_1, c_2)$  with  $|\alpha|, |\beta| < 1$ , are defined by

$$(33) \quad \ell_{(1, \alpha, \beta)}(c_1, c_2) : \begin{bmatrix} x_2 \\ x_3 \end{bmatrix} = \begin{bmatrix} \alpha x_1 + c_1 \\ \beta x_1 + c_2 \end{bmatrix} \quad c_1, c_2 \in \mathbb{Z}_{2n-1}, \quad x_1 \in \mathbb{Z}_n$$

To avoid wraparound, we can zero-pad  $f$  in a larger lattice  $\mathbb{Z}_p^3$  with  $p \geq 2n - 1$ . This is particularly important when it comes to define the ray transform by a line sum (cf. (39)-(41)) since wrap-around is unphysical. To fixed the idea, we define the object space that we shall work with:

$$(34) \quad \mathcal{X} := \{f \in O_n \text{ with the domain restricted to } \mathbb{Z}_{2n-1}^3\}.$$

Similarly, a  $x_2$ -line and a  $x_3$ -line are defined as

$$(35) \quad \ell_{(\alpha, 1, \beta)}(c_1, c_2) : \begin{bmatrix} x_1 \\ x_3 \end{bmatrix} = \begin{bmatrix} \alpha x_2 + c_1 \\ \beta x_2 + c_2 \end{bmatrix} \quad c_1, c_2 \in \mathbb{Z}_{2n-1}, \quad x_2 \in \mathbb{Z}_n,$$

$$(36) \quad \ell_{(\alpha, \beta, 1)}(c_1, c_2) : \begin{bmatrix} x_1 \\ x_2 \end{bmatrix} = \begin{bmatrix} \alpha x_3 + c_1 \\ \beta x_3 + c_2 \end{bmatrix} \quad c_1, c_2 \in \mathbb{Z}_{2n-1}, \quad x_3 \in \mathbb{Z}_n,$$

with  $|\alpha|, |\beta| < 1$ .

Let  $\tilde{f}$  be the continuous interpolation of  $f$  given by

$$(37) \quad \tilde{f}(x_1, x_2, x_3) = \sum_{i \in \mathbb{Z}_n} \sum_{j \in \mathbb{Z}_n} \sum_{k \in \mathbb{Z}_n} f(i, j, k) D_p(x_1 - i) D_p(x_2 - j) D_p(x_3 - k),$$

where  $D_p$  is the  $p$ -periodic Dirichlet kernel given by

$$(38) \quad D_p(t) = \frac{1}{p} \sum_{l \in \mathbb{Z}_p} e^{i2\pi lt/p} = \begin{cases} 1, & t = mp, \quad m \in \mathbb{Z} \\ \frac{\sin(\pi t)}{p \sin(\pi t/p)}, & \text{else.} \end{cases}$$

In particular,  $[D_p(i - j)]_{i, j \in \mathbb{Z}_p}$  is the  $p \times p$  identity matrix. Because  $D_p$  is a continuous  $p$ -periodic function, so is  $\tilde{f}$ . However, we will only use the restriction of  $\tilde{f}$  to one period cell  $[-(p-1)/2, (p-1)/2]^3$  to define the discrete projections and avoid the wraparound effect.

We define the discrete projections as the following line sums

$$(39) \quad f_{(1,\alpha,\beta)}(c_1, c_2) = \sum_{i \in \mathbb{Z}_n} \tilde{f}(i, \alpha i + c_1, \beta i + c_2),$$

$$(40) \quad f_{(\alpha,1,\beta)}(c_1, c_2) = \sum_{j \in \mathbb{Z}_n} \tilde{f}(\alpha j + c_1, j, \beta j + c_2)$$

$$(41) \quad f_{(\alpha,\beta,1)}(c_1, c_2) = \sum_{k \in \mathbb{Z}_n} \tilde{f}(\alpha k + c_1, \beta k + c_2, k)$$

with  $c_1, c_2 \in \mathbb{Z}_{2n-1}$ .

The 3D discrete Fourier transform  $\mathcal{F}f$  of the object  $f \in \mathcal{X}$ , is given by

$$(42) \quad \mathcal{F}f(\xi, \eta, \zeta) = p^{-3/2} \sum_{i,j,k} f(i, j, k) e^{-i2\pi(\xi i + \eta j + \zeta k)/p}$$

where the range of the Fourier variables  $\xi, \eta, \zeta$  can be extended from the discrete interval  $\mathbb{Z}_p$  to the continuum  $[-(p-1)/2, (p-1)/2]$ . Note that by definition,  $\hat{f}$  is a  $p$ -periodic band-limited function. When there is no risk of confusion, we shall denote the *full* DFT for 1D and 2D functions  $g$  by  $\mathcal{F}g$  and use the shorthand notation  $\hat{g} = \mathcal{F}g$ .

For  $z$ -lines, let  $\mathbf{t} = (\mathbf{t}', 1)$  with  $\mathbf{t}' = (\alpha, \beta)$  denote the direction vectors. Let  $\mathbf{f}_{\mathbf{t}}$  denote the discrete ray transform

$$(43) \quad \mathbf{f}_{\mathbf{t}}(c) := \sum_{j \in \mathbb{Z}_n} \mathbf{f}(\mathbf{t}'j + c, j_3), \quad \mathbf{c} = (c_1, c_2) \in \mathbb{Z}_p^2.$$

Let  $\mathcal{T}$  denote the set of directions  $\mathbf{t}$  employed in the 3D diffraction measurement with a coded aperture (Figure 1). To fix the idea, let  $p = 2n - 1$  in (38).

Let  $\mu$  be the mask function and  $f_{\mathbf{t}}$  the object projection in the direction  $\mathbf{t}$ .

The Fraunhofer diffraction of the masked scattered wave to the far-field detector in Figure 1 is modeled by the Fourier transform as

$$(44) \quad \mathcal{F}(\mathbf{f}_{\mathbf{t}} \odot \mu) = p^{-1} \hat{\mathbf{f}}_{\mathbf{t}} * \hat{\mu}(\mathbf{n}) := p^{-1} \sum_{\mathbf{n}' \in \mathbb{Z}_p^2} \hat{\mathbf{f}}_{\mathbf{t}}(\mathbf{n}') \hat{\mu}(\mathbf{n} - \mathbf{n}')$$

with the resulting coded diffraction patterns

$$(45) \quad \left\{ |\mathcal{F}(\mu \odot f_{\mathbf{t}})|^2, \quad \mathbf{t} \in \mathcal{T} \right\}.$$

Given the randomness assumption and the asymptotic nature of the reconstruction accuracy guaranteed by Theorem 2.1, it is expected that 1-bit phase retrieval with coded diffraction patterns is similarly asymptotic in the sense that the quality gradually increases as the numbers of diffraction patterns and random masks increase.

We decompose the signal process into two steps:

$$(46) \quad \mathcal{X} \xrightarrow{\mathcal{R}} \mathcal{X}_{\mathcal{T}} := \{(\mathbf{f}_{\mathbf{t}})_{\mathbf{t} \in \mathcal{T}} : \mathbf{f} \in \mathcal{X}\} \xrightarrow{\mathcal{Q}} \{p^{-1}(\hat{\mathbf{f}}_{\mathbf{t}} * \hat{\mu})_{\mathbf{t} \in \mathcal{T}} : \mathbf{f} \in \mathcal{X}\}$$



with the “collective” ray-transform  $\mathcal{R}$  and the masked 2D DFT  $\mathcal{Q}$ . Now we can write the noiseless signal model as  $b = |\mathcal{A}\mathbf{f}|$ , with the measurement matrix  $\mathcal{A} := \mathcal{Q}\mathcal{R}$ . The object domain projection  $\mathcal{P}_{\mathcal{X}}$  in Algorithm 1 is now carried out in the transform domain as

$$(47) \quad \mathcal{P} = \mathcal{A}\mathcal{A}^\dagger = \mathcal{Q}\mathcal{R}\mathcal{R}^\dagger\mathcal{Q}^*$$

where  $\mathcal{A}^\dagger$  and  $\mathcal{R}^\dagger$  are the pseudo-inverses of  $\mathcal{A}$  and  $\mathcal{R}$  on  $\mathcal{X}$ , respectively.

For simplicity, let us assume that  $\mu$  is a phase mask, i.e.  $\mu = \exp[i\phi]$ ,  $\phi \in \mathbb{R}$ . Then for each  $\mathbf{t}$  the mapping (44) of  $f_{\mathbf{t}}$  is an isometry, modulo a scale factor, while the tomographic mapping  $\mathcal{A}$  defined for the 3D object  $f$  is decisively not.

To avoid the missing cone problem in tomography, we consider  $m = 3\rho n$  evenly distributed random directions

$$(48) \quad \mathcal{T} = \{\mathbf{t}_i = (1, \alpha_i, \beta_i)\}_{i=1}^{\rho n} \cup \{\mathbf{t}_i = (\alpha_i, 1, \beta_i)\}_{i=1+\rho n}^{2\rho n} \cup \{\mathbf{t}_i = (\alpha_i, \beta_i, 1)\}_{i=2\rho n+1}^{3\rho n} \\ \text{with } \alpha_i, \beta_i, i = 1, \dots, 3\rho n, \text{ randomly chosen from } (-1, 1)$$

with the adjustable parameter  $\rho > 0$ .

## APPENDIX B. PSEUDO-INVERSE OF $\mathcal{A}$

We adopt the following notation:  $\mathcal{F}_i$ ,  $i = 1, 2, 3$ , denotes the 1D DFT in the  $i$ th variable over  $\mathbb{Z}_p$ ;  $\mathcal{F}_{ij}$ ,  $i, j = 1, 2, 3$ , denotes the 2D DFT in the  $i$ - and  $j$ -th variables over  $\mathbb{Z}_p^2$ ;  $\mathcal{F}$  denotes the 3D DFT over  $\mathbb{Z}_p^3$ . Let  $\mathcal{Z}$  denote the zero-padding operator,  $\mathcal{Z} : \mathbb{C}^{n \times n \times n} \rightarrow \mathbb{C}^{p \times p \times p}$ . Then its adjoint  $\mathcal{Z}^*$  is one projection,  $\mathcal{Z}^* : \mathbb{C}^{p \times p \times p} \rightarrow \mathbb{C}^{n \times n \times n}$ .

Since  $\mathcal{Q}^*\mathcal{Q} = I$ ,  $\mathcal{A}^\dagger = \mathcal{R}^\dagger\mathcal{Q}^*$  and hence the computation of  $\mathcal{A}^\dagger$  hinges on efficient implementation of  $\mathcal{R}^\dagger$ .

First consider the case of projections along  $z$ -lines only. We have

$$(49) \quad \begin{aligned} \mathbf{f}_{\mathbf{t}}(\mathbf{c}) &= \sum_{j \in \mathbb{Z}_n} \mathbf{f}(\mathbf{t}'j + \mathbf{c}, j) \\ &= p^{-2} \sum_{\mathbf{k}} \sum_{j \in \mathbb{Z}_n} \sum_{\mathbf{j}} f(\mathbf{j}, j) e^{i2\pi(\mathbf{t}'j + \mathbf{c} - \mathbf{j}) \cdot \mathbf{k}/p} \\ &= p^{-2} \sum_{\mathbf{k}} e^{i2\pi\mathbf{k} \cdot \mathbf{c}/p} \sum_{j \in \mathbb{Z}_n} e^{i2\pi j \mathbf{t}' \cdot \mathbf{k}/p} \sum_{\mathbf{j}} f(\mathbf{j}, j) e^{-2\pi\mathbf{k} \cdot \mathbf{j}/p} \\ &= p^{-1} \sum_{\mathbf{k}} e^{i2\pi\mathbf{k} \cdot \mathbf{c}/p} \sum_{j \in \mathbb{Z}_p} e^{i2\pi j \mathbf{t}' \cdot \mathbf{k}/p} \mathcal{F}_{12}(\mathcal{Z}\mathbf{f})(\mathbf{k}, j). \end{aligned}$$

For each  $g = (g_j) \in \mathbb{C}^p$ , let  $\Phi g$  be the quasi-periodic function given by

$$(50) \quad \Phi g(\zeta) = \sum_{j \in \mathbb{Z}^p} e^{i2\pi j \zeta/p} g_j, \quad g = (g_j) \in \mathbb{C}^p.$$

For given  $\mathbf{k}$  and  $\mathcal{T} = \{\mathbf{t}_l = (\mathbf{t}'_l, 1) : l = 1, \dots, m\}$  define the matrix  $\Psi$  by

$$(51) \quad \mathcal{K}g = \left( \Phi g(\mathbf{t}'_l \cdot \mathbf{k}) \right)_{l=1}^m, \quad g = (g_j) \in \mathbb{C}^p$$

whose adjoint is then given by

$$(52) \quad \mathcal{K}^* h = \left( \sum_{l=1}^m e^{-i2\pi j \mathbf{t}'_l \cdot \mathbf{k}/p} h_l \right)_{j \in \mathbb{Z}_p}, \quad h := (h_l) \in \mathbb{C}^m.$$

By (49)  $\mathcal{R}$  acting on  $\mathcal{X}$  can be decomposed as

$$(53) \quad \mathcal{R} = \mathcal{F}_{12}^* \mathcal{K} \mathcal{F}_{12} \mathcal{Z}.$$

Since

$$\mathcal{R}^\dagger = (\mathcal{R}^* \mathcal{R})^{-1} \mathcal{R}^*, \quad \mathcal{R}^* \mathcal{R} = \mathcal{Z}^* \mathcal{F}_{12}^* \Psi^* \Psi \mathcal{F}_{12} \mathcal{Z}$$

the key to computing  $\mathcal{R}^\dagger$  is the inversion of  $\mathcal{R}^* \mathcal{R}$ . Indeed, any

$$(54) \quad v := \mathcal{R}^\dagger h, \quad h \in \mathcal{X}_\mathcal{T} := \{(\mathbf{f}_t)_{t \in \mathcal{T}} : \mathbf{f} \in \mathcal{X}\}$$

satisfy the normal equation

$$(55) \quad \mathcal{Z}^* \mathcal{K}^* \mathcal{K} \mathcal{F}_{12} \mathcal{Z} v = \mathcal{Z}^* \mathcal{K}^* \mathcal{F}_{12} h$$

which is a Toeplitz system in view of the identity

$$(56) \quad \mathcal{K}^* \mathcal{K} \mathcal{F}_{12} \mathcal{Z} v(\mathbf{k}, j) = \sum_{i \in \mathbb{Z}_p} \sum_{l=1}^m e^{-i2\pi(j-i) \mathbf{t}'_l \cdot \mathbf{k}/p} \mathcal{F}_{12} \mathcal{Z} v(\mathbf{k}, i).$$

Observe that  $\mathcal{F}_{12} \mathcal{Z} v(\cdot, i) = 0$  for all  $i \notin \mathbb{Z}_n$  and  $i - j \in \mathbb{Z}_p$  for  $i, j \in \mathbb{Z}_n$  (with  $p = 2n - 1$ ). A Toeplitz matrix can be embedded into a circulant matrix, and the associated matrix-vector product can be implemented efficiently by FFTs [26] [5]. Hence  $\mathcal{K}^* \mathcal{K}$  can be implemented as a  $p \times p$  circulant matrix when acting on vectors supported on  $\mathbb{Z}_n$ :

$$(57) \quad \mathcal{K}^* \mathcal{K} = \left( \sum_{l=1}^m e^{-i2\pi(j-i) \mathbf{t}'_l \cdot \mathbf{k}/p} \right)_{i, j \in \mathbb{Z}_p}.$$

Consequently,  $\mathcal{Z}^* \Psi^* \Psi \mathcal{Z}$  can be efficiently inverted by diagonalizing with FFT. This fast matrix-vector product motivates the adoption of conjugate gradient (CG) methods for computing  $(\mathcal{R}^* \mathcal{R})^{-1}$ .

Indeed, let

$$(58) \quad w(\mathbf{k}, k) := \sum_{l=1}^m e^{-i2\pi k \mathbf{t}'_l \cdot \mathbf{k}/p}, \quad (\mathbf{k}, k) \in \mathbb{Z}_p^3.$$

By (56) and the discrete convolution theorem

$$(59) \quad \mathcal{K}^* \mathcal{K} \mathcal{F}_{12} \mathcal{Z} v = w *_3 \mathcal{F}_{12} \mathcal{Z} v = \sqrt{p} \mathcal{F}_3^* (\mathcal{F}_3 w \odot \mathcal{F}_3 \mathcal{F}_{12} \mathcal{Z} v)$$

where  $*_3$  denotes the discrete convolution over the third variable. Hence

$$(60) \quad \mathcal{F}_{12}^* \mathcal{K}^* \mathcal{K} \mathcal{F}_{12} \mathcal{Z} v = \sqrt{p} \mathcal{F}^* (\mathcal{F}_3 w \odot \mathcal{F} \mathcal{Z} v).$$

By (55), any  $v = \mathcal{R}^\dagger h, h \in \mathcal{X}_\mathcal{T}$  satisfy

$$(61) \quad \mathcal{R}^* \mathcal{R} v = \sqrt{p} \mathcal{Z}^* \mathcal{F}^* (\mathcal{F}_3 w \odot \mathcal{F} \mathcal{Z} v) = \mathcal{Z}^* \mathcal{F}_{12}^* \mathcal{K}^* \mathcal{F}_{12} h, \quad v \in \mathcal{X},$$

which is then solved by CG in the space  $\mathcal{X}$ .

In summary, we have  $A^\dagger = \mathcal{R}^\dagger \mathcal{Q}^*$  where  $\mathcal{R}^\dagger$  is obtained by solving eq. (61) with  $w$  given by (58).

### APPENDIX C. $\mathcal{A}^\dagger$ WITH $x$ -, $y$ - AND $z$ -LINES

Let

$$(62) \quad \mathcal{T}_1 = \{\mathbf{t}_i = (1, \alpha_i, \beta_i) \in \mathbb{R}^3 : i = 1, \dots, m_1\}$$

$$(63) \quad \mathcal{T}_2 = \{\mathbf{t}_i = (\alpha_i, 1, \beta_i) \in \mathbb{R}^3 : i = m_1 + 1, \dots, m_1 + m_2\}$$

$$(64) \quad \mathcal{T}_3 = \{\mathbf{t}_i = (\alpha_i, \beta_i, 1) \in \mathbb{R}^3 : i = m_1 + m_2 + 1, \dots, m_1 + m_2 + m_3\}$$

and  $\mathcal{T} = \mathcal{T}_1 \cup \mathcal{T}_2 \cup \mathcal{T}_3$  be the total set of  $m = m_1 + m_2 + m_3$  projection directions.

Let  $\mathcal{A}_j = \mathcal{Q}_j \mathcal{R}_j$  be the partial measurement matrix and decomposition corresponding to  $\mathcal{T}_j, j = 1, 2, 3$ . Let  $\mathcal{A} = [\mathcal{A}_1^T, \mathcal{A}_2^T, \mathcal{A}_3^T]^T$  be the full measurement matrix which can be decomposed as  $\mathcal{A} = \mathcal{Q} \mathcal{R}$  where  $\mathcal{Q} = \text{diag}[\mathcal{Q}_1, \mathcal{Q}_2, \mathcal{Q}_3]$  is the collective masked Fourier transform and  $\mathcal{R} = [\mathcal{R}_1^T, \mathcal{R}_2^T, \mathcal{R}_3^T]^T$  the collective ray transform.

To compute  $\mathcal{A}^\dagger = \mathcal{R}^\dagger \mathcal{Q}^\dagger$  the key is  $\mathcal{R}^\dagger$ . Since  $\mathcal{R}^\dagger = (\mathcal{R}^* \mathcal{R})^{-1} \mathcal{R}^*$ , we have

$$(65) \quad \mathcal{R}^\dagger = (\mathcal{R}_1^* \mathcal{R}_1 + \mathcal{R}_2^* \mathcal{R}_2 + \mathcal{R}_3^* \mathcal{R}_3)^{-1} \mathcal{R}^*.$$

Analogous to (53), we have

$$\begin{aligned} \mathcal{R}_1 &= \mathcal{F}_{23}^* \mathcal{K}_1 \mathcal{F}_{23} \mathcal{Z} \\ \mathcal{R}_2 &= \mathcal{F}_{13}^* \mathcal{K}_2 \mathcal{F}_{13} \mathcal{Z} \\ \mathcal{R}_3 &= \mathcal{F}_{12}^* \mathcal{K}_3 \mathcal{F}_{12} \mathcal{Z}. \end{aligned}$$

where for any  $g = (g_j) \in \mathbb{C}^p$

$$\begin{aligned} \mathcal{K}_1 g &= \left( \Phi g(\alpha_l k_2 + \beta_l k_3) \right)_{l=1}^{m_1} \\ \mathcal{K}_2 g &= \left( \Phi g(\alpha_l k_1 + \beta_l k_3) \right)_{l=m_1+1}^{m_1+m_2} \\ \mathcal{K}_3 g &= \left( \Phi g(\alpha_l k_1 + \beta_l k_2) \right)_{l=m_1+m_2+1}^m \end{aligned}$$

with the transform  $\Phi$  defined by (50). Hence by (65), the key to  $\mathcal{R}^\dagger$  is to invert the operator

$$(66) \quad \mathcal{R}^* \mathcal{R} = \mathcal{Z}^* (\mathcal{F}_{23}^* \mathcal{K}_1^* \mathcal{K}_1 \mathcal{F}_{23} + \mathcal{F}_{13}^* \mathcal{K}_2^* \mathcal{K}_2 \mathcal{F}_{13} + \mathcal{F}_{12}^* \mathcal{K}_3^* \mathcal{K}_3 \mathcal{F}_{12}) \mathcal{Z}.$$

Observe that from the discrete convolution theorem, we have

$$(67) \quad \mathcal{R}^* \mathcal{R} v = \sqrt{p} \mathcal{Z}^* \mathcal{F}^* \left( u \odot \mathcal{F} \mathcal{Z} v \right), \quad u := \sum_{l=1}^3 \mathcal{F}_l w_l,$$

where  $\mathcal{R}^* = [\overline{\mathcal{R}_1}, \overline{\mathcal{R}_2}, \overline{\mathcal{R}_3}]$  (over-line denotes complex conjugation) and

$$(68) \quad w_1(k_1, k_2, k_3) = \sum_{l=1}^{m_1} e^{-i2\pi k_1(k_2\alpha_l + k_3\beta_l)/p},$$

$$(69) \quad w_2(k_1, k_2, k_3) = \sum_{l=m_1+1}^{m_1+m_2} e^{-i2\pi k_2(k_1\alpha_l + k_3\beta_l)/p},$$

$$(70) \quad w_3(k_1, k_2, k_3) = \sum_{l=m_1+m_2+1}^m e^{-i2\pi k_3(k_1\alpha_l + k_2\beta_l)/p}.$$

Analogous to (61), we solve for  $v = \mathcal{R}^\dagger h$  from the equation:

$$(71) \quad \sqrt{p} \mathcal{Z}^* \mathcal{F}^* (u \odot \mathcal{F} \mathcal{Z} v) = \mathcal{R}^* h.$$

#### APPENDIX D. PRECONDITIONERS

We shall employ preconditioned conjugate gradient methods (PCG) to solve (20), where the preconditioner is a circulant preconditioner related to  $\mathcal{R}^* \mathcal{Q}^* \mathcal{Q} \mathcal{R} = \mathcal{R}^* \mathcal{R}$ . Suppose that all entries of  $u$  in (67) are positive. One natural preconditioner is Strang's circulant preconditioner  $\mathcal{M}$  satisfying

$$(72) \quad \mathcal{M}^{-1} v = p^{-1/2} \mathcal{Z}^* \mathcal{F}^* \{u^{-1} \odot \mathcal{F}(\mathcal{Z} v)\}, \quad v \in \mathcal{X}.$$

Unfortunately, even though  $\mathcal{R}^* \mathcal{R}$  is positive definite, these entries in  $u$  vary widely, and some of them are negative. To alleviate the difficulty, we introduce a minor but necessary modification:

$$(73) \quad \mathcal{M}^{-1} v = p^{-1/2} \mathcal{Z}^* \mathcal{F}^* \{u^{-1} \odot \mathcal{F}(\mathcal{Z} v) \odot (u \geq \epsilon)\},$$

where  $\epsilon$  is chosen to be a small positive scalar with  $\mathcal{M} \succ 0$ . In simulations,  $\epsilon = 0.1$  is used.

#### APPENDIX E. KRYLOV SUBSPACE METHODS TO COMPUTE THE SECOND EIGENVECTOR

For a large Hermitian matrix, the Krylov subspace method is one efficient approach to compute eigenvectors of the extreme values. [13, 14, 22] For instance, we can employ the block Lanczos algorithm in 10.3.6 in [13] to compute a few extreme eigenvectors of  $\mathcal{S}^{-1} \mathcal{S}_\omega$ . The following illustrates one algorithm that can efficiently compute the first two dominant eigenvectors of  $\mathcal{S}^{-1} \mathcal{S}_\omega$ .

Let  $l$  be an integer with  $l \geq 2$ . Let  $\mathbf{f}$  denote an  $N \times l$  matrix, consisting of the first  $l$  dominant eigenvectors of  $\mathcal{S}^{-1} \mathcal{S}_\omega$ . Then  $\mathbf{f}$  can be regarded as a solution to

$$(74) \quad \max_{\mathbf{f}} \{\mathcal{G}(\mathbf{f}) := \langle \mathbf{f}, \mathcal{S}_\omega \mathbf{f} \rangle\}, \text{ subject to } \mathbf{f}^* \mathbf{S} \mathbf{f} = I_l.$$

Apply the Rayleigh–Ritz method to get Ritz approximation of (74). Construct a Krylov subspace spanned by the column space of some full rank matrix  $X$ . Consider the low dimensional approximate  $\mathbf{f}$  in (74),  $\mathbf{f} \approx X\beta$ . Then  $\beta$  is a maximizer to

$$(75) \quad \max_{\beta} \langle X\beta, \mathcal{S}_\omega X\beta \rangle \text{ subject to } \beta^* X^* \mathcal{S} X \beta = I_l.$$

The following illustrates the determination of  $\beta$ .

**Proposition E.1.** *Let  $X$  be some  $N \times k$  matrix with rank  $k \geq l$ . Introduce  $C_{S_\omega} := X^* \mathcal{S}_\omega X$ ,  $C_S := X^* \mathcal{S} X$ . Suppose  $\mathbf{f} = X\beta$  for some  $\beta \in \mathbb{C}^{k \times l}$ . Then  $\beta$  satisfies the maximization problem:*

$$(76) \quad \max_{\beta} \langle X\beta, \mathcal{S}_\omega X\beta \rangle = \max_{\beta} \langle \beta, C_{S_\omega} \beta \rangle$$

subject to

$$(77) \quad \beta^* X^* \mathcal{S} X \beta = \beta^* C_S \beta = I_l.$$

The optimal solution is  $\beta = C_S^{-1/2} \alpha$ , where  $\alpha$  is the matrix whose columns are the first  $l$  dominant eigenvectors of  $C_S^{-1/2} C_{S_\omega} C_S^{-1/2}$ .

*Proof.* First, from (77), we express  $\beta = C_S^{-1/2} \alpha$  for some unitary  $k \times l$  matrix  $\alpha$ , i.e.,  $\alpha^* \alpha = I_l$ . Second, from (76),  $\alpha$  is a maximizer of

$$(78) \quad \max_{\alpha} \langle C_S^{-1/2} \alpha, C_{S_\omega} C_S^{-1/2} \alpha \rangle.$$

Obviously, the optimal choice on  $\alpha$  is the matrix whose columns are the first  $l$  dominant eigenvectors of  $C_S^{-1/2} C_{S_\omega} C_S^{-1/2}$ .  $\square$

As noted in section 3.1, the shifted inverse iteration converges faster than the power iteration. We shall apply the operator  $(I - \mathcal{S}^{-1} \mathcal{S}_\omega)^{-1}$  to reach the invariant subspace of  $\mathcal{S}^{-1} \mathcal{S}_\omega$ , i.e.,  $\text{span}\{f_1, \dots, f_l\}$ . This constructed subspace is known as the shift-and-invert Krylov subspace [8], which was introduced for the calculation of the matrix exponential acting on a vector.

In summary, we repeat the two-step iterative procedure to reach a maximizer of  $\mathcal{G}(\mathbf{f})$  in (74):

- Let  $\mathbf{f} = [f_1, \dots, f_l] \in \mathbb{C}^{n \times l}$ . Form  $X \in \mathbb{C}^{n \times lp}$ , whose columns are
- $$(79) \quad \cup_{j=1, \dots, l} \{f_j, ((\mathcal{S} - \mathcal{S}_\omega)^{-1} \mathcal{S}) f_j, \dots, ((\mathcal{S} - \mathcal{S}_\omega)^{-1} \mathcal{S})^{p-1} f_j\}.$$
- Update  $f$  with  $\mathbf{f} = [f_1, \dots, f_l] = X\beta$ , where  $\beta$  is determined from Prop. E.1.

#### ACKNOWLEDGEMENT

The research PC is supported in part by grants 110-2115-M-005 -007 -MY3 and 111-2918-I-005 -002 from the National Science and Technology Council, Taiwan. The research of AF is supported in part by the Simons Foundation grant FDN 2019-24 and the US National Science Foundation grant CCF-1934568.

## REFERENCES

- [1] A. Averbuch & Y. Shkolnisky, “3D discrete X-ray transform,” *Appl. Comput. Harmon. Anal.* **17** (2004) 259-276.
- [2] D.P Bertsekas, “On the Goldstein-Levitin-Polyak gradient projection method,” *IEEE Trans. Auto. Contr.* **21** (1976) 174-184.
- [3] D.P. Bertsekas, *Nonlinear Programming*, Athena Scientific, Belmont, MA, 2016.
- [4] R. H. T. Bates, B. K. Quek, and C. R. Parker, “Some implications of zero sheets for blind deconvolution and phase retrieval,” *J. Opt. Soc. Am. A* **7** (1990) 468-479.
- [5] R. H.F Chan and X.Q. Jin, *An Introduction to Iterative Toeplitz Solvers (Fundamentals of Algorithms)*. 2007.
- [6] P. Chen, A. Fannjiang, G. Liu, “Phase retrieval by linear algebra,” *SIAM J. Matrix Anal. Appl.* **38** (2017) 854 - 868.
- [7] S. Curtis, S. Shitz and A.V. Oppenheim, “Reconstruction of nonperiodic two-dimensional signals from zero crossings,” *IEEE Trans. Acoust. Speech Signal Proc.* **35** (1987) 890-893.
- [8] J. van den Eshof and M. Hochbruck, “Preconditioning lanczos approximations to the matrix exponential,” *SIAM Journal on Scientific Computing* **27** (2006) 1438-1457.
- [9] A. Fannjiang, “Absolute uniqueness of phase retrieval with random illumination,” *Inverse Problems* **28** (2012) 075008.
- [10] A. Fannjiang, “Uniqueness theorems for tomographic phase retrieval with few coded diffraction patterns”, *Inverse Problems* **38** (2022) 085008.
- [11] A. Fannjiang, “3D tomographic phase retrieval and unwrapping,” *Inverse Problems* **40** (2024) 015015
- [12] J. Frank, *Three-Dimensional Electron Microscopy of Macromolecular Assemblies*, 2nd edition, Oxford University Press, New York, 2006.
- [13] G.H. Golub and C.F. Van Loan. *Matrix Computations*. Johns Hopkins Studies in the Mathematical Sciences. Johns Hopkins University Press, 2013.
- [14] G.H. Golub and Q. Ye. “An inverse free preconditioned Krylov subspace method for symmetric generalized eigenvalue problems,” *SIAM Journal on Scientific Computing* **24** (2002) 312-334.
- [15] R. Hegerl and W. Hoppe, “Influence of electron noise on three-dimensional image reconstruction,” *Zeitschrift für Naturforschung* **31 a** (1976), 1717-1721.
- [16] R. Henderson, “The potential and limitations of neutrons, electrons and X-rays for atomic resolution microscopy of unstained biological molecules.” *Quarterly Reviews of Biophysics* **28(2)** (1995), 171-193.
- [17] W. Hoppe and R. Hegerl, “Some remarks concerning the influence of electron noise on 3D reconstruction,” *Ultramicroscopy* **6** (1981), 205-206.
- [18] M.R. Howells, T. Beetz, H.N. Chapman, C. Cuia, J.M. Holton, C.J. Jacobsena, J. Kirz, E. Lima, S. Marchesini, H. Miao, D. Sayre, D.A. Shapiro, J.C.H. Spence, D. Starodub, “An assessment of the resolution limitation due to radiation-damage in X-ray diffraction microscopy.” *Journal of Electron Spectroscopy and Related Phenomena* **170** (2009), 4-12.
- [19] C. Jacobsen, *X-ray Microscopy*, Cambridge University Press, 2020.
- [20] B.F. McEwen, K.H. Downing, & R.M. Glaeser, “The relevance of dose-fractionation in tomography of radiation-sensitive specimens.” *Ultramicroscopy* **60** (1995) 357-373.
- [21] A. Rose, “Unified approach to performance of photographic film, television pickup tubes, and human eye,” *J. Soc. Motion Picture Eng.* **47** (1946), 273-294.
- [22] Y. Saad, *Iterative Methods for Sparse Linear Systems*. PWS Publishing Company, Boston, 1996.
- [23] J.L.C. Sanz and T. T. Huang, “Image representation by sign information” *IEEE Trans. Pattern Anal. Machine Intel.* **11 (7)** (1989) 729-738.
- [24] M.S. Scivier and M.A. Fiddy, “Phase ambiguity and the zeros of multidimensional band-limited functions,” *J. Opt. Soc. Am. A* **2** (1985) 693-697.
- [25] Q. Shen, W. Leitenberger & P. Thibault, “Modes of three-dimensional imaging with coherent X-ray diffraction.” *Journal of Synchrotron Radiation* **11** (2004), 432-438.
- [26] G. Strang. “A proposal for toeplitz matrix calculations,” *Studies in Appl. Math.* **74** (1986) 171-176.

- [27] Z. Wang, A. C. Bovik, H. R. Sheikh, and E. P. Simoncelli, "Image quality assessment: From error visibility to structural similarity," *IEEE Trans. Image Process.* **13** (2004), pp. 600-612.
- [28] A. Zakhor & A.V. Oppenheim, "Reconstruction of two-dimensional signals from level crossings," *Proceedings of the IEEE* **78** (1990) 31-55.